Preprint typeset in JINST style - HYPER VERSION

Hadronic energy resolution of a highly granular scintillator-steel hadron calorimeter using software compensation techniques

The CALICE Collaboration

C. Adloff, J. Blaha, J.-J. Blaising, C. Drancourt, A. Espargilière, R. Gaglione, N. Geffroy, Y. Karyotakis, J. Prast, G. Vouters

Laboratoire d'Annecy-le-Vieux de Physique des Particules, Université de Savoie, CNRS/IN2P3, 9 Chemin de Bellevue BP110, F-74941 Annecy-le-Vieux CEDEX, France

K. Francis, J. Repond, J. Schlereth, J. Smith[*], L. Xia

Argonne National Laboratory, 9700 S. Cass Avenue, Argonne, IL 60439-4815, USA

E. Baldolemar, J. Li[†], S. T. Park, M. Sosebee, A. P. White, J. Yu

Department of Physics, SH108, University of Texas, Arlington, TX 76019, USA

T. Buanes, G. Eigen

University of Bergen, Inst. of Physics, Allegaten 55, N-5007 Bergen, Norway

Y. Mikami, N. K. Watson

University of Birmingham, School of Physics and Astronomy, Edgbaston, Birmingham B15 2TT, UK

G. Mavromanolakis[‡], M. A. Thomson, D. R. Ward, W. Yan[§]

University of Cambridge, Cavendish Laboratory, J J Thomson Avenue, CB3 0HE, UK

D. Benchekroun, A. Hoummada, Y. Khoulaki

Université Hassan II Aïn Chock, Faculté des sciences. B.P. 5366 Maarif, Casablanca, Morocco

M. Benyamna, C. Cârloganu, F. Fehr, P. Gay, S. Manen, L. Royer

Clermont Univertsité, Université Blaise Pascal, CNRS/IN2P3, LPC, BP 10448, F-63000 Clermont-Ferrand, France

G. C. Blazey, A. Dyshkant, J. G. R. Lima, V. Zutshi

NICADD, Northern Illinois University, Department of Physics, DeKalb, IL 60115, USA

J. -Y. Hostachy, L. Morin

Laboratoire de Physique Subatomique et de Cosmologie - Université Joseph Fourier Grenoble 1 - CNRS/IN2P3 - Institut Polytechnique de Grenoble, 53, rue des Martyrs, 38026 Grenoble CEDEX, France

U. Cornett, D. David, G. Falley, K. Gadow, P. Göttlicher, C. Günter, B. Hermberg, S. Karstensen, F. Krivan, A. -I. Lucaci-Timoce[‡], S. Lu, B. Lutz, S. Morozov, V. Morgunov[¶], M. Reinecke, F. Sefkow, P. Smirnov, M. Terwort, A. Vargas-Trevino

DESY, Notkestrasse 85, D-22603 Hamburg, Germany

N. Feege, E. Garutti, I. Marchesini[‖], M. Ramilli
Univ. Hamburg, Physics Department, Institut für Experimentalphysik, Luruper Chaussee 149, 22761 Hamburg, Germany

P. Eckert, T. Harion, A. Kaplan, H. -Ch. Schultz-Coulon, W. Shen, R. Stamen
University of Heidelberg, Fakultat fur Physik und Astronomie, Albert Uberle Str. 3-5 2.OG Ost, D-69120 Heidelberg, Germany

B. Bilki, E. Norbeck, Y. Onel
University of Iowa, Dept. of Physics and Astronomy, 203 Van Allen Hall, Iowa City, IA 52242-1479, USA

G. W. Wilson
University of Kansas, Department of Physics and Astronomy, Malott Hall, 1251 Wescoe Hall Drive, Lawrence, KS 66045-7582, USA

K. Kawagoe
Department of Physics, Kyushu University, Fukuoka 812-8581, Japan

P. D. Dauncey, A. -M. Magnan
Imperial College London, Blackett Laboratory, Department of Physics, Prince Consort Road, London SW7 2AZ, UK

M. Wing
Department of Physics and Astronomy, University College London, Gower Street, London WC1E 6BT, UK

F. Salvatore[**]
Royal Holloway University of London, Dept. of Physics, Egham, Surrey TW20 0EX, UK

E. Calvo Alamillo, M.-C. Fouz, J. Puerta-Pelayo
CIEMAT, Centro de Investigaciones Energeticas, Medioambientales y Tecnologicas, Madrid, Spain

V. Balagura, B. Bobchenko, M. Chadeeva, M. Danilov, A. Epifantsev, O. Markin, R. Mizuk, E. Novikov, V. Rusinov, E. Tarkovsky
Institute of Theoretical and Experimental Physics, B. Cheremushkinskaya ul. 25, RU-117218 Moscow, Russia

N. Kirikova, V. Kozlov, P. Smirnov, Y. Soloviev
P. N. Lebedev Physical Institute, Russian Academy of Sciences, 117924 GSP-1 Moscow, B-333, Russia

P. Buzhan, B. Dolgoshein, A. Ilyin, V. Kantserov, V. Kaplin, A. Karakash, E. Popova, S. Smirnov
Moscow Physical Engineering Inst., MEPhI, Dept. of Physics, 31, Kashirskoye shosse, 115409 Moscow, Russia

C. Kiesling, K. Seidel, F. Simon[♠], C. Soldner, M. Szalay, M. Tesar, L. Weuste
Max Planck Inst. für Physik, Föhringer Ring 6, D-80805 Munich, Germany

J. Bonis, B. Bouquet, S. Callier, P. Cornebise, Ph. Doublet, F. Dulucq, M. Faucci Giannelli, J. Fleury, H. Li,[‡†] G. Martin-Chassard, F. Richard, Ch. de la Taille, R. Pöschl, L. Raux, N. Seguin-Moreau, F. Wicek

Laboratoire de l'Accélérateur Linéaire, Centre Scientifique d'Orsay, Université de Paris-Sud XI, CNRS/IN2P3, BP 34, Bâtiment 200, F-91898 Orsay CEDEX, France

M. Anduze, V. Boudry, J-C. Brient, D. Jeans, P. Mora de Freitas, G. Musat, M. Reinhard, M. Ruan, H. Videau

Laboratoire Leprince-Ringuet (LLR) – École Polytechnique, CNRS/IN2P3, F-91128 Palaiseau, France

B. Bulanek, J. Zacek

Charles University, Institute of Particle & Nuclear Physics, V Holesovickach 2, CZ-18000 Prague 8, Czech Republic

J. Cvach, P. Gallus, M. Havranek, M. Janata, J. Kvasnicka, D. Lednicky, M. Marcisovsky, I. Polak, J. Popule, L. Tomasek, M. Tomasek, P. Ruzicka, P. Sicho, J. Smolik, V. Vrba, J. Zalesak

Institute of Physics, Academy of Sciences of the Czech Republic, Na Slovance 2, CZ-18221 Prague 8, Czech Republic

B. Belhorma, H. Ghazlane

Centre National de l'Energie, des Sciences et des Techniques Nucléaires, B.P. 1382, R.P. 10001, Rabat, Morocco

T. Takeshita, S. Uozumi

Shinshu Univ. , Dept. of Physics, 3-1-1 Asaki, Matsumoto-shi, Nagano 390-861, Japan

M. Götze, O. Hartbrich, J. Sauer, S. Weber, C. Zeitnitz

Bergische Universität Wuppertal Fachbereich 8 Physik, Gaussstrasse 20, D-42097 Wuppertal, Germany

♠ *Corresponding author*
E-mail: fsimon@mpp.mpg.de

ABSTRACT: The energy resolution of a highly granular 1 m^3 analogue scintillator-steel hadronic calorimeter is studied using charged pions with energies from 10 GeV to 80 GeV at the CERN SPS. The energy resolution for single hadrons is determined to be approximately $58\%/\sqrt{E/\mathrm{GeV}}$. This resolution is improved to approximately $45\%/\sqrt{E/\mathrm{GeV}}$ with software compensation techniques. These techniques take advantage of the event-by-event information about the substructure of hadronic showers which is provided by the imaging capabilities of the calorimeter. The energy reconstruction is improved either with corrections based on the local energy density or by applying a single correction factor to the event energy sum derived from a global measure of the shower energy density. The application of the compensation algorithms to GEANT4 simulations yield resolution improvements comparable to those observed for real data.

KEYWORDS: hadronic calorimetry; imaging calorimetry; software compensation.

Contents

1. Introduction

The physics goals of future high-energy lepton colliders such as the ILC [1] or CLIC [2] put stringent requirements on the detector systems. For example, the efficient event-by-event separation of heavy bosons in hadronic final states requires a jet energy resolution of better than 4% [1]. This is achievable with Particle Flow Algorithms (PFA) combined with highly granular calorimeters [3, 4, 5]. The CALICE collaboration has constructed and extensively studied highly granular electromagnetic and hadronic calorimeter prototypes to evaluate detector technologies for future linear collider experiments. These calorimeters have been successfully operated in various test beam experiments in different configurations at DESY, CERN and Fermilab from 2006 until 2012. The unprecedented granularity of the CALICE calorimeter prototypes allows the structure of hadronic showers to be studied with high spatial resolution, in order to validate different simulation

[*] Also at University of Texas, Arlington

[†] Deceased

[‡] Now at CERN

[§] Now at Dept. of Modern Physics, Univ. of Science and Technology of China, 96 Jinzhai Road, Hefei, Anhui, 230026, P. R. China

[¶] On leave from ITEP

[‖] Also at DESY

[**] Now at University of Sussex, Physics and Astronomy Department, Brighton, Sussex, BN1 9QH, UK

[††] Now at LPSC Grenoble

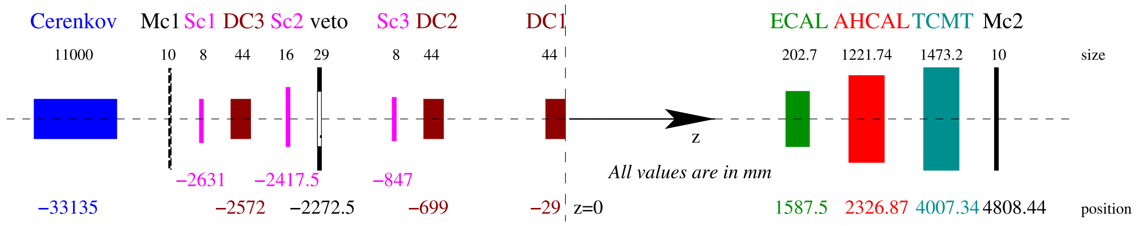

Figure 1. Top view of the CALICE test beam apparatus in the CERN SPS H6 beam line including calorimeters, trigger components (scintillator triggers SC1, SC2, and SC3; large area muon trigger counters Mc1, which was used only during calibration runs, and Mc2; and the beam halo veto), and the tracking drift chambers DC1, DC2, and DC3. The beam enters from the left. Dimensions are in millimeters. Figure is not to scale. Position are given at detector center.

models (for one example of such studies see [6]) and to test particle flow algorithms, as demonstrated in [7]. The high granularity also offers the possibility for advanced energy reconstruction methods, the subject of this paper.

We present a study of the hadronic energy resolution of the CALICE analogue scintillator-steel hadronic calorimeter (AHCAL) [8] using data taken at the CERN SPS in 2007 with positive and negative pion beams in the energy range from 10 to 80 GeV. Two software compensation techniques, which weight energy depositions based on information about the local energy density within the shower obtained from the highly granular readout, are discussed in detail. Both techniques achieve an improvement of the hadronic energy resolution by approximately 20% for single hadrons in the energy range from 10 to 80 GeV, with a reduction of the stochastic term from $\sim 58\%/\sqrt{E/\mathrm{GeV}}$ to $\sim 45\%/\sqrt{E/\mathrm{GeV}}$.

In Section 2 we briefly describe the test beam setup, discuss the event selection and describe the energy reconstruction, calibration and the determination of the energy resolution in the AHCAL. The software compensation techniques are presented in Section 3, and Section 4 summarizes the results obtained from data which are compared to simulation.

2. Energy reconstruction in the AHCAL

2.1 Test beam setup

The complete CALICE setup in the H6 beam line at the CERN SPS for the 2007 beam period, illustrated in Figure 1, consisted of a silicon-tungsten electromagnetic sampling calorimeter (ECAL) [9], the AHCAL, and a scintillator-steel tail catcher and muon tracker (TCMT) [10]. The test beam setup was also equipped with various trigger and beam monitoring devices.

The ECAL has a total depth of 24 radiation lengths (approximately 1 nuclear interaction length λ_I) and consists of 30 active silicon layers arranged in three longitudinal sections with different absorber thicknesses. In this study, the ECAL was used for event selection and early shower detection. Since the present study focuses on the AHCAL, events with a primary inelastic interaction in the ECAL were rejected, as discussed below.

The AHCAL consists of small 5 mm thick plastic scintillator tiles with individual readout by silicon photomultipliers (SiPMs). The tiles are assembled in 38 layers with lateral dimensions of 900×900 mm^2, separated by 21 mm of steel. The absorber material in each layer is made up by 17 mm thick absorber plates and two 2 mm thick cover plates of the cassettes that house the scintillator cells. The size of the scintillator tiles ranges from 30×30 mm^2 in the central region and 60×60 mm^2 in the outer region to 120×120 mm^2 along the perimeter of each layer. In the last eight layers only 60×60 mm^2 and 120×120 mm^2 tiles are used. In total, the CALICE AHCAL has 7608 scintillator cells and a thickness of 5.3 λ_I (4.3 λ_π).

The TCMT consists of 16 readout layers assembled from 5 mm thick, 50 mm wide and 1000 mm long scintillator strips read out by SiPMs. The scintillator is sandwiched between steel absorber plates. The TCMT has two sections with different sampling fractions, one fine section with 21 mm thick absorbers for the first 9 layers, and a coarse section with 104 mm thick absorbers. 2 mm of the absorber thickness in each layer is provided by the cover sheets of the scintillator strip cassettes. In this study the information from the TCMT is used for muon separation and to measure energy leaking out of the back of the AHCAL, which is of particular importance at higher energies. The total depth of CALICE calorimeter setup amounts to approximately 12 λ_I, with a total of 17 648 readout channels.

In addition to the calorimeters themselves, the setup includes auxiliary detectors for triggering, tracking and particle identification as shown in Figure 1. The scintillation counters Sc1, Sc2 and Sc3 provide the beam trigger, where a coincidence between at least two out of the three is required. In addition, Sc2 has an analogue readout to tag multi-particle events. The large area veto counter is used to reject beam halo events and a large area scintillator counter Mc2 downstream of the TCMT to provide muon tagging for particles penetrating the full calorimeter setup. For dedicated muon runs, an additional large area scintillation counter, Mc1, is installed upstream of the calorimeters. Three drift chambers DC1, DC2 and DC3 determine the position of the incoming beam particles. Particle identification is provided by a threshold Čerenkov counter upstream of the calorimeters, used to discriminate between electrons and pions or between pions and protons in negatively or positively charged beams, respectively.

2.2 Event selection

The response of the individual calorimeter cells are calibrated with muons, using the visible signal of a minimum-ionizing particle (MIP) as the cell-to-cell calibration scale. After this cell-to-cell calibration, the most probable energy loss of a MIP is used as the base unit of the energy measurement. To reject noise, only cells with a visible energy above a threshold of 0.5 MIP are used in the analysis, referred to as hits in the following.

The data samples for the present analysis are selected from π^- and π^+ data in the energy range of 10 to 80 GeV and 30 to 80 GeV respectively, as summarised in Table 1. To maximise statistics, data from several run periods taken at different temperatures are combined for most energies, with corrections for the temperature dependence of the photon sensor applied during event reconstruction. The goal of the event selection procedure is the purification of the pion samples by rejecting admixtures of muons as well as electrons or protons. To identify muons, information from the ECAL, AHCAL and TCMT is used, requiring low deposited energy consistent with a minimum-ionizing particle in all three detectors. Optimal separation of muons and hadrons is

particle type	beam energy [GeV]	all pions	selected pions
π^-	10	440208	84706
π^-	15	127554	24997
π^-	18	52880	10492
π^-	20	342798	67093
π^-	25	201243	39631
π^-	35	272987	54126
π^-	40	472345	93301
π^-	45	325092	63547
π^-	50	304023	59076
π^-	60	647090	121588
π^-	80	741440	139248
π^+	30	155210	30884
π^+	40	307177	60595
π^+	50	159414	30843
π^+	60	449273	86947
π^+	80	272441	52442

Table 1. Summary of the data samples. The total number of pions is the number of events classified as pions, after rejection of empty, noisy and double particle events, and the application of muon rejection and particle identification cuts. The number of selected pions are the events with an identified shower start in the first five layers of the AHCAL, which are used in the present analysis. For most energies, several run periods at different temperatures are combined to maximise statistics.

achieved by using beam energy-dependent dependent constraints on the energy sum in the TCMT versus the combined energy sum of the ECAL and AHCAL. For beam energies of 30 GeV and 35 GeV a muon contamination at the level of 30% and 15%, is observed, respectively, while for all other energies the muon content does not exceed 7%. After the event selection, the muon content is below 0.5% at all energies, estimated using the muon identification efficiency of 98% at 10 GeV and 99.5% GeV at 30 GeV and above, which is determined from muon data and simulations. Protons and kaons are removed from the π^+ samples by requiring a positive pion identification in the Čerenkov counter. Electrons are removed from the π^- sample both by the Čerenkov counter and by selecting events with no inelastic interaction in the ECAL, as discussed below.

Since the goal of the present analysis is the study of the performance of the AHCAL, pion showers that develop predominantly in the AHCAL are selected. This is achieved by requiring that the position of the primary inelastic interaction is located in the first five layers of the hadron calorimeter. This excludes events with sizable energy deposit in the ECAL while keeping energy leakage into the TCMT to a minimum. The location of the primary inelastic interaction is determined by detecting the change from a minimum-ionizing particle track to multiple secondary particles, evidenced by an increased energy deposition and number of hits over several consecutive layers [7]. Simulation studies indicate that the difference between the reconstructed and the true primary interaction layer does not exceed one layer for 78% of all events and does not exceed two layers for more than 90% of all events in the energy range from 10 to 80 GeV.

2.3 Energy reconstruction and intrinsic energy resolution

To obtain the deposited energy in the sub-detectors, a conversion from the visible signal in MIP units to the total energy in units of GeV is necessary. Since only hadrons with a shower start in the AHCAL are considered, the relevant conversion factor for the ECAL is determined using simulated muons to obtain the correlation between the visible energy and true ionization energy loss in the detector. This factor is validated with the measured response to muons obtained from a sample of muon data. The sampling fraction for minimum-ionizing particles is approximately 25% higher than that for electromagnetic showers, resulting in a lower conversion factor than that for electrons presented in [11]. The total energy deposited in the AHCAL is obtained at the electromagnetic scale, using calibration factors determined for electron and positron data [12]. Since the AHCAL is a non-compensating calorimeter, the response to hadrons differs from that to electrons, requiring an additional scaling factor. It was determined by comparing the reconstructed energy for pions using the electromagnetic calibration factors with the known beam energy. In the present study, the energy dependence of this factor is ignored by taking a constant $\frac{e}{\pi} = 1.19$, corresponding to the average over the energy range studied. Since the first nine TCMT layers are essentially identical to the AHCAL layers in terms of absorber and active material, the same electromagnetic calibration factors and an identical $\frac{e}{\pi}$ ratio are assumed. For the last seven TCMT layers, the calibration factors are adjusted according to the increased absorber thickness.

For each event, the uncorrected reconstructed energy for hadrons, E_{unc}, is given by the sum of reconstructed energies in the three calorimeters,

$$E_{\mathrm{unc}} = E_{\mathrm{ECAL}}^{\mathrm{track}} + \frac{e}{\pi} \cdot (E_{\mathrm{HCAL}} + E_{\mathrm{TCMT}}) , \qquad (2.1)$$

where $E_{\mathrm{ECAL}}^{\mathrm{track}}$ is the measured energy in the ECAL deposited by the particle track, and E_{HCAL} and E_{TCMT} are the energies measured in the AHCAL and in the TCMT, both given at the electromagnetic scale. The energy in each subdetector is given by the sum of all hits above a noise threshold of 0.5 MIP.

The resulting reconstructed energy distributions are fitted with a Gaussian in the interval of ± 2 standard deviations around the mean value, providing good fits with a $\chi^2/\mathrm{NDF} < 2$ for all energies. The differences compared to a fit over the full range are on the few per mille level for the extracted mean and on the one percent level for standard deviation and depend on the beam energy. Fitting over the full range reduces the fit quality for some energies in particular for the uncorrected data, leading to the choice of of ± 2 standard deviations for best consistency between the different data points. In the following, the mean and standard deviation of this Gaussian fit at a given beam energy are referred to as the mean reconstructed energy E_{reco} and the resolution σ_{reco}, respectively. Systematic uncertainties on the energy measurement in the AHCAL are discussed in detail in [12]. For the reconstruction of hadrons, the main source of systematic uncertainties is the uncertainty of the MIP to GeV conversion factor that is extracted from the electromagnetic calibration of the detector. The size of the uncertainty was studied thoroughly for the present data set, and is determined to be 0.9% by varying the calibration constants within the allowed limits. Other effects which contribute to the uncertainties for electromagnetic showers, such as the saturation behaviour of the photon sensor, are found to be negligible for hadrons even at the highest energies studied here.

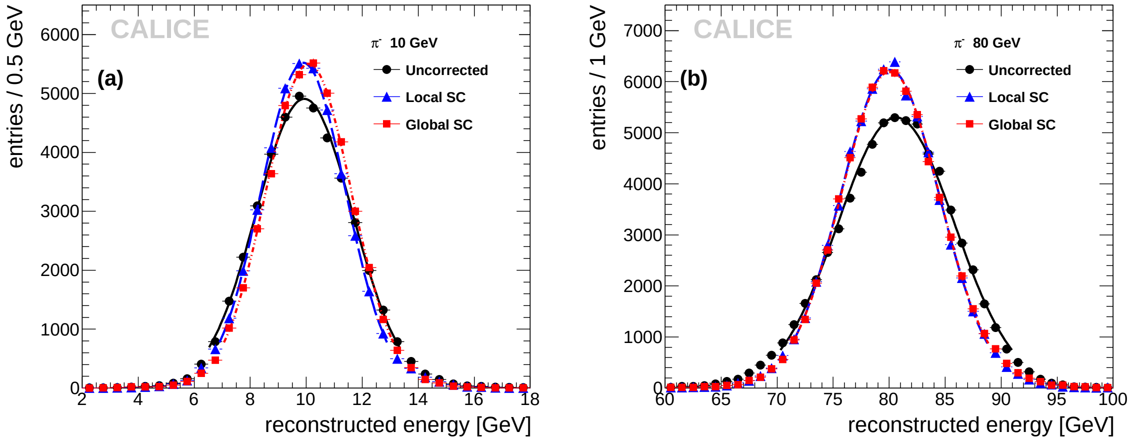

Figure 2. Reconstructed energy distributions for 10 GeV π^- (a) and 80 GeV π^- (b) without compensation (black circles) and after local software compensation (LC), shown by the blue triangles, and after global software compensation (GC), shown by the red squares. The curves show Gaussian fits to the distributions in the range of ± 2 standard deviations. Errors are statistical only.

Figure 2 shows the distribution of reconstructed energies for 10 GeV and 80 GeV pions, with the uncorrected reconstructed energy shown by black data points. At all energies, the distributions of the reconstructed energies follow a Gaussian distribution well, with typically more than 95% of all events in the fit range of ± 2 standard deviations. The software compensation methods also included in the figure are described in Sections 3.1 (local software compensation) and 3.2 (global software compensation).

Figure 3 shows the mean reconstructed energy versus beam energy, with the black points giving the uncorrected reconstructed energy. The measured responses to positive and negative pions agree well within the systematic uncertainties, which are shown by the green band. Relative residuals to the beam energy are shown in the lower panel of Figure 3. The linearity of the calorimeter response to hadrons is within $\pm 2\%$ in the studied energy range.

The fractional energy resolution, $\sigma_{\text{reco}}/E_{\text{reco}}$, is shown in Figure 4. Again, the uncorrected relative resolution is indicated by black points. The measured resolution for π^- is in very good agreement with that obtained for π^+, with the differences smaller than the size of the markes for all energies where both π^- and π^+ results exist. The black solid curve shows the result of a fit to these points with the following function:

$$\frac{\sigma_{\text{reco}}}{E_{\text{reco}}} = \frac{a}{\sqrt{E_{\text{beam}}}} \oplus b \oplus \frac{c}{E_{\text{beam}}}, \tag{2.2}$$

where E_{beam} is the beam energy in GeV, and a, b and c are the stochastic, constant and noise contributions, respectively. The noise term is fixed to $c = 0.18$ GeV, corresponding to the measured noise contribution in the full CALICE setup taking into account contributions from the ECAL (0.004 GeV), the AHCAL (0.06 GeV) and the TCMT (0.17 GeV). These values are obtained from the standard deviation of the noise levels measured in dedicated runs without beam particles as well as in random trigger events constantly recorded during data taking. From the fit, the

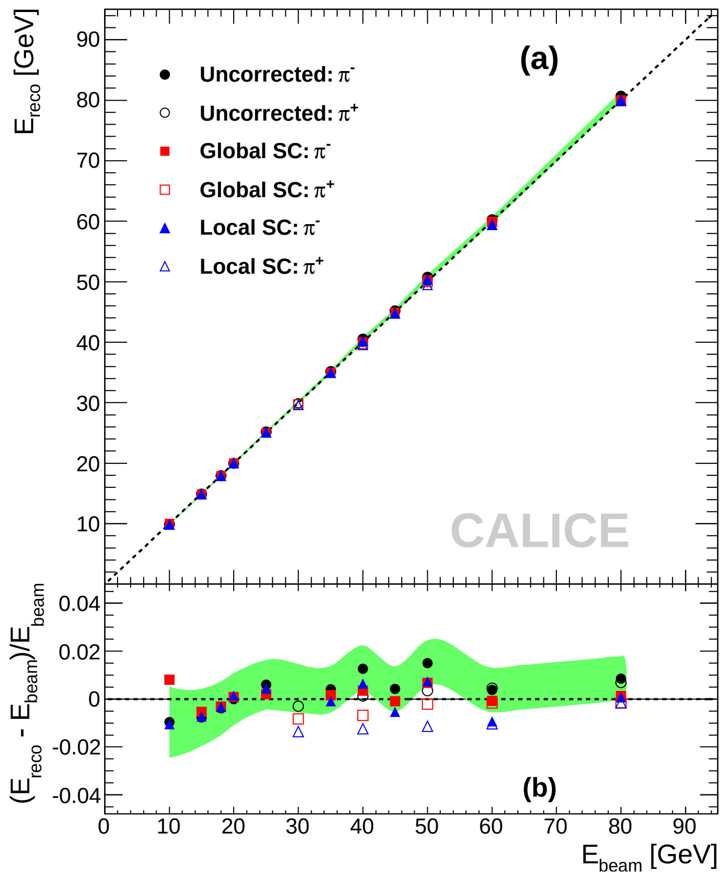

Figure 3. (a) Mean reconstructed energy for pions and (b) relative residuals to beam energy versus beam energy without compensation (black circles) and after local software compensation (LC), shown by the blue triangles, and after global software compensation (GC), shown by the red squares. Filled and open markers indicate π^- and π^+, respectively. Dotted lines correspond to $E_{\mathrm{reco}} = E_{\mathrm{beam}}$. Systematic uncertainties are indicated by the green band, which corresponds to the uncertainties for the uncorrected π^- data sample.

stochastic term of the uncorrected hadron energy resolution of the AHCAL is determined to be $(57.6 \pm 0.4)\%/\sqrt{E/\mathrm{GeV}}$ and the constant term to be $(1.6 \pm 0.3)\%$.

3. Software compensation: motivation and techniques

In ideal sampling calorimeters the energy measured for electromagnetic showers is directly proportional to the incoming particle energy. In the absence of instrumental effects such as non-linearities or saturation of the readout, the energy of a particle can thus be obtained by multiplying the visible signal by a single energy-independent factor accounting for the non-measured energy depositions in the passive absorber material.

The calorimeter response to hadron-induced showers is more complicated [13], since these showers have contributions from two different components: an electromagnetic component, origi-

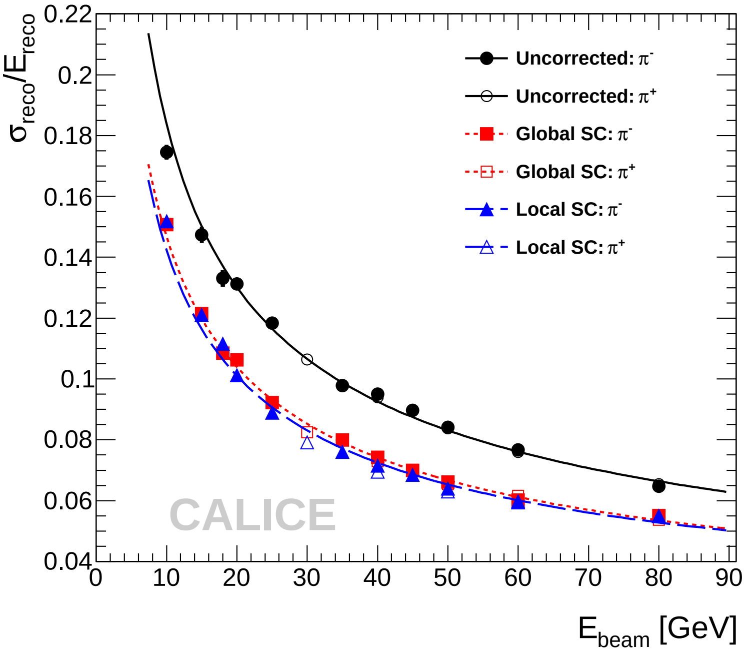

Figure 4. Relative energy resolution versus beam energy without compensation and after local and global software compensation. The curves show fits using Equation 2.2, with the black solid line showing the fit to the uncorrected resolution, the red dotted line to global software compensation and the blue dashed line to local software compensation. The stochastic term is $(57.6 \pm 0.4)\%$, $(45.8 \pm 0.3)\%$ and $(44.3 \pm 0.3)\%$, with constant terms of $(1.6 \pm 0.3)\%$, $(1.6 \pm 0.2)\%$ and $(1.8 \pm 0.3)\%$ for the uncorrected resolution, global software compensation and local software compensation, respectively.

nating primarily from the production of π^0s and ηs and their subsequent decay into photon pairs; and a purely hadronic component. The latter includes "invisible" components from the energy loss due to the break-up of absorber nuclei, from low-energy particles absorbed in passive material and from undetected neutrons, depending on the active material. This typically leads to a reduced response of the calorimeter to energy in the hadronic component, and thus overall to a smaller calorimeter response to hadrons compared to electromagnetic particles of the same energy. Since the production of π^0s and ηs are statistical processes, the relative size of the two shower components fluctuates from shower to shower, which, combined with the differences in visible signal for electromagnetic and purely hadronic energy deposits, leads to a deterioration of the energy resolution. In addition, the average fraction of energy in the electromagnetic component depends on the number of subsequent inelastic hadronic interactions and thus on the initial particle energy. The electromagnetic fraction of hadronic showers increases with increasing particle energy [14], often resulting in a non-linear response for non-compensating calorimeters.

There are two fundamentally different approaches to improve the energy resolution of a hadronic sampling calorimeter. One approach is to eliminate the issue of different response to electromagnetic and hadronic components by design, through the construction of so-called compensating calorimeters. This can be achieved by specific choices of absorber and active material which enhance the sensitivity to neutrons, and thus to the hadronic component of the shower, and by appropriately chosen sampling fractions. However, these conditions impose very strict requirements on the materials used and on the overall geometry of the whole detector system. One prominent example of a compensating calorimeter is the uranium-scintillator calorimeter of the ZEUS experiment [15, 16], which reached a stochastic resolution term of $34.5\%/\sqrt{E/\mathrm{GeV}}$ for single pions [17].

On the other hand, for intrinsically non-compensating calorimeters, compensation can be achieved by so-called "off-line weighting" or "software compensation" techniques. These techniques assign different weights to electromagnetic and hadronic energy deposits on an event-by-event basis. The different spatial structure of the electromagnetic and hadronic components of particle showers can be used to characterize the origin of energy deposits. Since the radiation length is much shorter than the nuclear interaction length in heavy absorbers used in hadronic calorimeters, electromagnetic sub-showers are more compact than purely hadronic sub-showers, generally resulting in a higher energy density of the electromagnetic component. The application of software compensation techniques relies on longitudinal and lateral segmentation of the calorimeters, to provide the necessary information for a measurement of the energy density of particle showers. One of the first applications of such techniques was in the WA1/CDHS scintillator steel calorimeter, where an improvement of the hadronic resolution between 10% and 30% was achieved in the energy range of 10 GeV to 140 GeV [18]. These techniques were further refined and applied in various experiments, such as the H1 liquid argon calorimeter [19] and the ATLAS calorimeter system [20].

With its unprecedented high granularity, the CALICE AHCAL is well suited for such techniques. In the present paper, two techniques based on an event-by-event analysis of the hit energy distributions are discussed. The local software compensation (LC) procedure is based on a re-weighting of each individual hit depending on the local energy density. The global software compensation (GC) procedure uses the distribution of hit energies to derive one global factor for the correction of the reconstructed energy of the complete hadronic shower. The parameters used for both techniques are determined from test beam data, as discussed in detail below. The available data set is split into two samples of equal event count, a training data set and the data set used to study the energy reconstruction. This ensures a statistical independence of the data used to determine the parameters for the software compensation algorithms and the data used to evaluate the performance of the techniques.

3.1 Local software compensation

The local software compensation technique improves the energy reconstruction for hadrons by applying weights to the energy recorded in every cell of the AHCAL within a hadronic shower. The weights are chosen based on the local energy density, which is taken as a measure of the likelihood a given cell belongs to an electromagnetic or a hadronic sub-shower. In the present study, the energy content of a cell, divided by its volume, is taken as the relevant local energy density. Electromagnetic sub-showers typically have a higher energy density than purely hadronic ones, and, due to the non-compensating nature of the AHCAL, result in a larger detector signal per unit of deposited energy. Thus, cells with a higher energy content are assigned a lower weight in the global energy sum than cells with a low energy content to correct for this difference. The

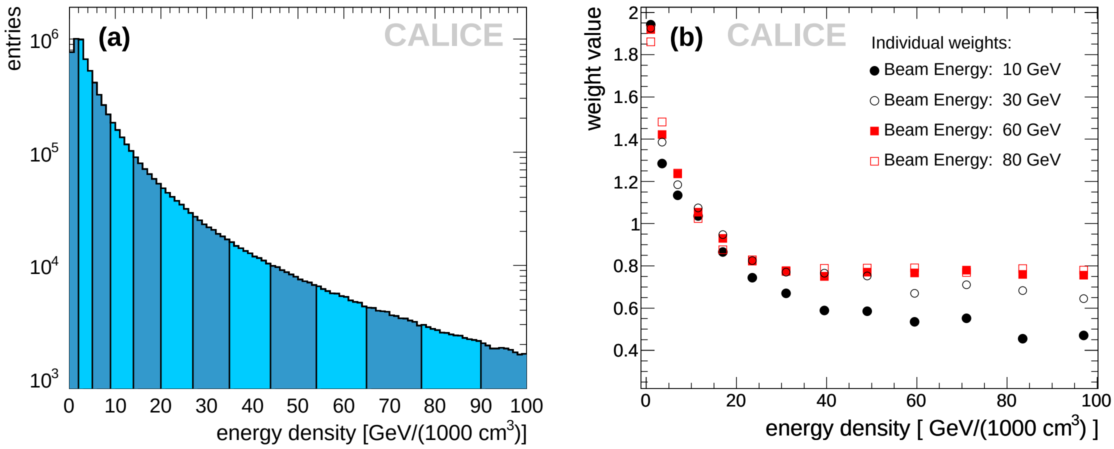

Figure 5. (a) Distribution of the cell energy density in the AHCAL for 20 GeV pion showers. The different energy density bins used in the analysis are indicated by color shades. (b) Optimal weights as a function of energy density for different beam energies, determined without constraints of a specific functional form in the first iteration of the minimization.

reconstructed energy of each event corrected with local software compensation, E_{LC}, is thus given by introducing weights for each AHCAL hit in Equation 2.1, resulting in

$$E_{\mathrm{LC}} = E_{\mathrm{ECAL}}^{\mathrm{track}} + \frac{e}{\pi} \cdot \left(\sum_i (E_{\mathrm{HCAL},i} \cdot \omega_i) + E_{\mathrm{TCMT}} \right) \tag{3.1}$$

where ω_i is the energy density dependent weight applied to the cell energy $E_{\mathrm{HCAL},i}$.

To make the technique robust against fluctuations, the single cell energy density distribution is subdivided into bins in energy density, as illustrated in Figure 5 (a). For each bin, a separate weight is determined which is applied to all hits that fall into that particular bin. The number of sub-divisions in energy density is chosen as a compromise between the requirements for fine subdivisions to maximize the sensitivity of the algorithm to differences in shower structure on one hand, and the stability of the determination of the weights and of the algorithm on the other hand. While a fine binning improves the sensitivity to the shower structure, a robust determination of the weights requires sufficient statistics in each bin, and changes of the weights from bin to bin.

Since the overall energy density of hadronic showers changes with energy, the weights ω depend both on the cell energy density ρ and on the particle energy. The weights, as a function of energy density and particle energy, are determined from the training data set extending over the full energy range studied here. The optimal weights are found by minimizing a simplified χ^2 given by the function $\chi^2 = \sum_i (E_{\mathrm{LC},i} - E_{\mathrm{beam}})^2$, where $E_{\mathrm{LC},i}$ is the reconstructed energy of a given event using software compensation, and the sum runs over all events used for the weight determination. In this minimization, the bin by bin weights are used as free parameters. Figure 5 (b) shows the optimal weights determined with this procedure for four different energies. The weights at a given beam energy can be parametrized by

$$\omega = p_0 + p_1 \cdot \exp(p_2 \cdot \rho), \tag{3.2}$$

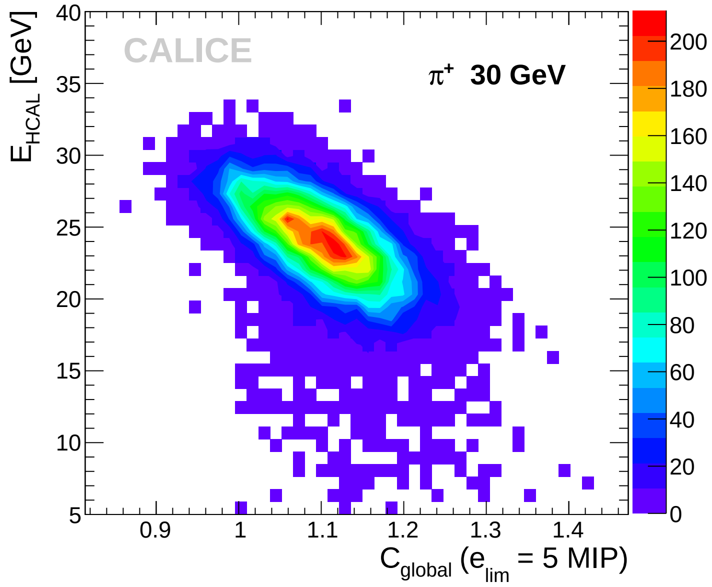

Figure 6. Correlation of the factor C_{global} and the reconstructed energy in the AHCAL, E_{HCAL}, for showers induced by π^+ at 30 GeV.

where ρ is the energy density corresponding to the centre of the energy density bins introduced above, and p_0, p_1 and p_2 are parameters of the weight function. These parameters depend on the beam energy, with their energy dependence following exponential functions in particle energy for p_0 and p_1, and a logarithmic function in particle energy for p_2. A robust determination of the weights is achieved by an iterative minimization procedure, where the free parameters p_0, p_1 and p_2 are consecutively fixed to the function determined in the previous minimization stage.

For the application of this technique to data, no *a priori* knowledge of the particle energy is required, as the uncorrected reconstructed particle energy is used instead of E_{beam} to select the correct weight parametrization. Since the energy dependence of the weight parameters is not very steep, this does not introduce a noticeable bias for the reconstructed energy. A second iteration does not lead to significant further improvement and is thus not performed in the reconstruction.

3.2 Global software compensation

The global software compensation technique improves the energy resolution for hadrons by applying a single weight to the reconstructed shower energy. This weight is derived from the distribution of hit energies in the hadronic shower, providing sensitivity to the overall energy density, and thus to the fraction of hits in electromagnetic sub-showers. Since electromagnetic sub-showers are characterized by a high local energy density, a hadronic shower with a large electromagnetic content will have a larger fraction of high-energy hits than a shower with predominantly hadronic contributions.

The determination of the event weight is based on a phenomenological approach using the fraction of calorimeter hits below a certain energy threshold, which serves as a measure for the importance of low-density energy deposits, and thus of predominantly hadronic origin, in a given event. Based on this, with an additional consideration of the overall hit energy distribution given by the number of hits below the mean energy value of the hit energy, the factor C_{global} is constructed, which is used to correct the reconstructed energy. This factor, calculated for each event, is given by the ratio of the number of shower hits with a measured visible signal below a given threshold e_{lim} and the number of shower hits with a measured visible signal below the mean value of the hit energy spectrum for that particular event. Figure 6 illustrates the sensitivity of the factor C_{global} to the reconstructed energy, for a value of e_{lim} = 5 MIP applied to π^+ events at 30 GeV. The clear anti-correlation between the reconstructed energy and C_{global} provides the basis for an improved energy reconstruction using this factor. The anti-correlation is due to the fact that events with a high electromagnetic content tend to have a larger number of high-energy hits above e_{lim} and thus a lower C_{global}, while those events have a higher reconstructed energy.

The value of e_{lim} was optimized to provide good performance of the algorithm over the full energy range, with the linearity of the detector response taken as a key factor. While higher values for e_{lim} provide stricter separation of electromagnetic and non-electromagnetic events, if the value is set too high this results in asymmetric distributions of C_{global} at lower energy, leading to reduced performance. These asymmetries originate from the reduced number of high-energy hits at low particle energies. For example, a large fraction of 10 GeV pion showers have essentially no hits above 7 MIP. Too low values, on the other hand, result in a non-linear response due to the reduced sensitivity to the electromagnetic component at higher particle energies. Best performance was obtained for a value of e_{lim} = 5 MIP. For the energy range studied, the mean hit energy is between 2.7 to 4.7 MIP. Figure 7 shows the distributions of C_{global} for different energies, demonstrating its energy dependence, originating from the change of the overall hit energy spectrum with changing particle energy. When applying C_{global} in the energy reconstruction, this dependence has to be corrected for, as discussed below.

The reconstructed energy with global software compensation is obtained in two steps. First, a corrected shower energy is calculated by multiplying the reconstructed energy in the AHCAL and in the TCMT with the factor C_{global}, giving $E_{\mathrm{shower}} = C_{\mathrm{global}}\,(E_{\mathrm{HCAL}} + E_{\mathrm{TCMT}})$. From this corrected shower energy, the final reconstructed energy with global software compensation for a given event, E_{GC}, is then obtained from

$$E_{\mathrm{GC}} = E_{\mathrm{ECAL}}^{\mathrm{track}} + E_{\mathrm{shower}} \cdot P_{\mathrm{global}}(E_{\mathrm{shower}}), \tag{3.3}$$

where $P_{\mathrm{global}}(E_{\mathrm{shower}})$ is a function which accounts for the energy dependence of the compensation parameters, visible in Figure 7 by the shift of the mean of C_{global} with energy. This function depends on the corrected shower energy E_{shower} and is given by a second-order polynomial, $P_{\mathrm{global}}(E_{\mathrm{shower}}) = a_0 + a_1 \cdot E_{\mathrm{shower}} + a_2 \cdot E_{\mathrm{shower}}^2$. The parameters for this function are obtained from a fit of the dependence of the corrected shower energy E_{shower} on the true deposited energy given by the beam energy corrected for the energy deposited in the ECAL, and are extracted from a training data set extending over the full energy range considered here.

The application of the global software compensation technique does not require knowledge of the beam energy, since the energy reconstructed in the HCAL and TCMT is used also in the determination of the correction of the energy dependence of the compensation parameters.

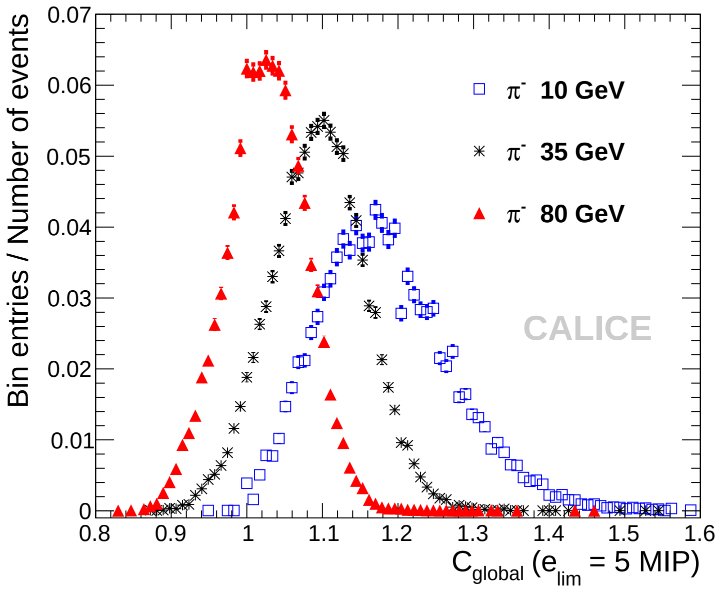

Figure 7. Distributions of the factor C_{global} for hadronic showers induced by π^- with an energy of 10 GeV (blue squares), 35 GeV (black circles) and 80 GeV (red triangles), respectively. Statistical errors are shown.

4. Results

To evaluate their performance, both software compensation techniques are applied to test beam data and to simulated data. The parameters for the algorithms are determined using test beam data following the training procedures outlined above.

4.1 Application of software compensation to test beam data

When applying the software compensation techniques to test beam data, the energy dependent compensation factors are determined event-by-event using the uncorrected reconstructed energy. Figure 2 shows the distribution of reconstructed energies for the uncorrected reconstruction compared with both studied software compensation techniques. The results are shown for pions with energies of 10 GeV and 80 GeV. In both cases, the software compensation algorithms improve the energy resolution, evidenced by a narrowing of the distributions, while preserving or even improving the Gaussian form of the distributions. The algorithms also bring the mean value of the reconstructed energy closer to the beam energy, resulting in small shifts of the maxima visible in Figure 2. The mean reconstructed energy with local and global compensation techniques, compared to the uncorrected response without compensation, is shown in Figure 3 for all energies studied. For both techniques, all points fall within $\pm 1.5\%$ of linearity.

The relative energy resolution before and after compensation is shown in Figure 4. Good agreement between the π^- and π^+ samples is observed. The energy dependence of the relative resolution is well described by Equation 2.2 with a fixed noise term $c = 0.18$ GeV as discussed in Section 2.3. The fit results are summarized in Table 2. The application of software compensation results in a decrease of the stochastic term while the constant term remains unchanged. Both

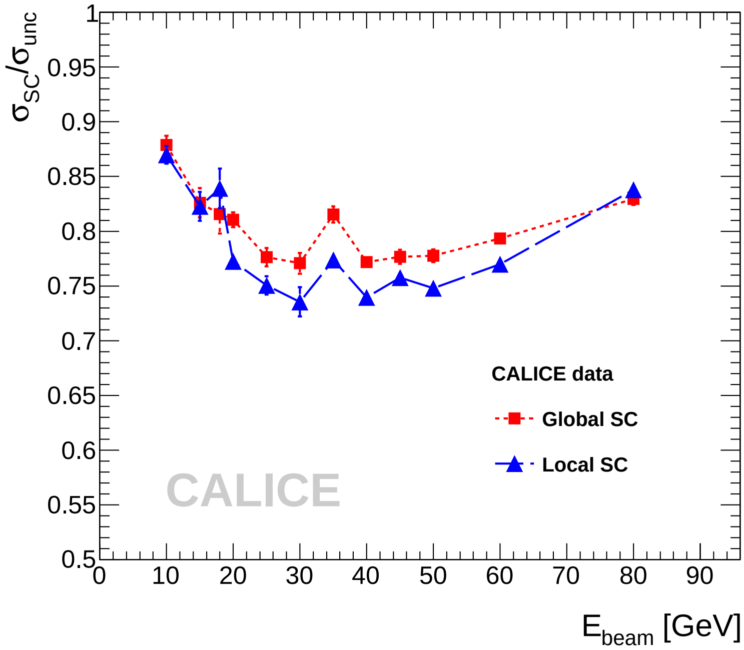

Figure 8. Energy dependence of the relative improvement of the resolution with local and global software compensation observed for data. Where available, results for π^- and π^+ are averaged for clarity.

compensation techniques show very similar performance, with the local software compensation providing a slightly smaller stochastic term, and slightly better performance at intermediate energies. This larger improvement of the resolution, in particular for the 30 GeV point, leads to the increased χ^2 of the fit in the case of the local software compensation, as apparent from Figure 4.

Table 2. Stochastic, constant and noise term contributions to the resolution of the CALICE AHCAL determined with a fit of Equation (2.2).

Resolution	a, %	b, %	c, GeV	χ^2/NDF
Uncorrected	57.6±0.4	1.6±0.3	0.18	3.6
Local compensation	44.3±0.3	1.8±0.2	0.18	8.0
Global compensation	45.8±0.3	1.6±0.2	0.18	2.6

Figure 8 shows the relative improvement of the energy resolution achieved with the software compensation techniques, defined as the ratio of the resolution after software compensation σ_{SC} (local or global) and the uncorrected resolution σ_{unc}. The improvement ranges from ~12% to ~25% in the energy range studied for both techniques, with approximately 3% better relative improvement observed for the local technique in the energy range from 25 GeV to 60 GeV. The reduced performance at high energy is partially due to increased leakage into the TCMT. Energy deposits in the TCMT are not weighted in the local software compensation since their energy density is not well defined. In the global software compensation, the weight is applied also to TCMT

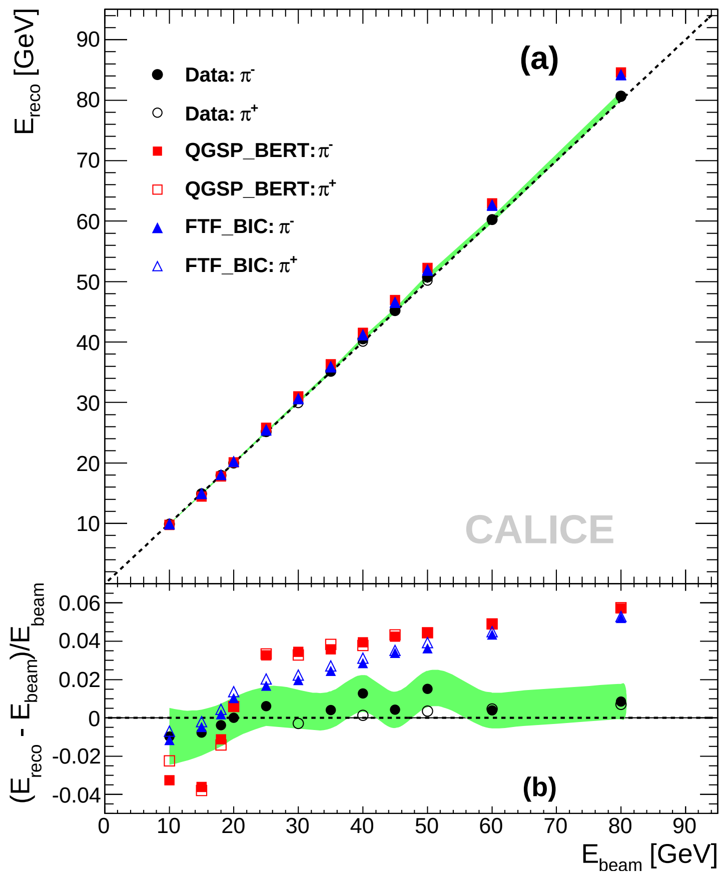

Figure 9. (a) Uncorrected response to pions and (b) relative residuals to beam energy versus beam energy for data (black circles), QGSP_BERT (red squares) and FTF_BIC (blue triangles). Filled and open markers indicate π^- and π^+, respectively. Dotted lines correspond to $E_{\text{reco}} = E_{\text{beam}}$, while the green band shows systematic uncertainties for the uncorrected π^- data sample.

energy deposits, but those are not considered in the determination of the weighting factor due to the different readout geometry which leads to increased uncertainties in the weight determination.

4.2 Comparison to Monte Carlo simulations

The stability of both software compensation techniques, as well as the realism of simulation models, is tested using Monte Carlo simulations. For this purpose, the software compensation algorithms with coefficients derived from data are applied to Monte Carlo samples generated with a detailed detector model in GEANT4.9.4 [21] using two physics lists: QGSP_BERT and FTF_BIC [22]. The QGSP_BERT physics list was chosen because it is the most widely used model in high energy physics experiments at present. The FTF_BIC physics list, in turn, has provided good results in a previous CALICE analysis [6] and is completely independent from QGSP_BERT.

Details on the simulation procedure for the AHCAL can be found in [12]. For the chosen

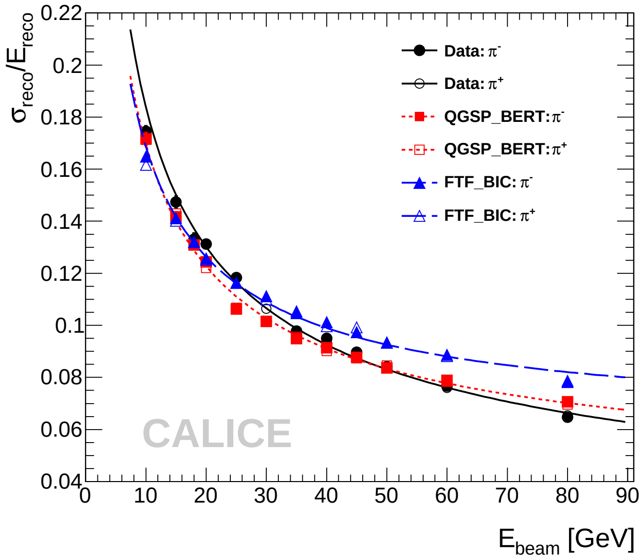

Figure 10. Uncorrected relative resolution versus beam energy for data as well as simulations using the physics lists QGSP_BERT and FTF_BIC. The curves show fits using Equation 2.2. The stochastic terms are $(57.6 \pm 0.4)\%$, $(51.8 \pm 0.3)\%$ and $(49.4 \pm 0.3)\%$, with constant terms of $(1.6 \pm 0.3)\%$, $(4.0 \pm 0.1)\%$ and $(6.1 \pm 0.1)\%$ for data, QGSP_BERT and FTF_BIC, respectively.

physics lists, samples of π^+ and π^- events were simulated at the same energies as the data points, using beam profiles, detector temperatures and voltage settings from the data runs. The calibration of the simulation was performed at the MIP level by converting the simulated energy deposits in the scintillator into MIPs using the most probable energy loss of muons determined in simulations. The simulated data sets were passed through the same event selection and reconstruction procedures as real data, using the conversion factors from the MIP scale to reconstructed energy determined for data as discussed in Section 2.3.

The uncorrected reconstructed energy as a function of beam energy is shown for data and both physics lists in Figure 9 (a). The relative deviation from the beam energy, shown in Figure 9 (b), indicates that simulations with both physics lists behave different from data. Both models show an overestimation of the reconstructed energy at high particle energies. In addition, QGSP_BERT exhibits fluctuations in the transition region between different models in the region between 10 GeV and 20 GeV. In general, the reconstructed energy for simulations is less linear than for data.

Figure 10 shows the energy resolution without software compensation, comparing data and simulations. Again, the behaviour of simulations is different from that of the data, with both models underestimating the resolution at low energy, and with FTF_BIC overestimating the resolution above 30 GeV. This difference leads to a reduced stochastic resolution term with a significantly increased constant term.

The effect of the application of the software compensation algorithms with parameters extracted from data on the reconstructed energy in simulations is shown in Figure 11. For both techniques, the under-estimation of the detector response at low energy, in particular by the QGSP_BERT physics list, remains present. At intermediate energies from 20 GeV up to 50 GeV, the applica-

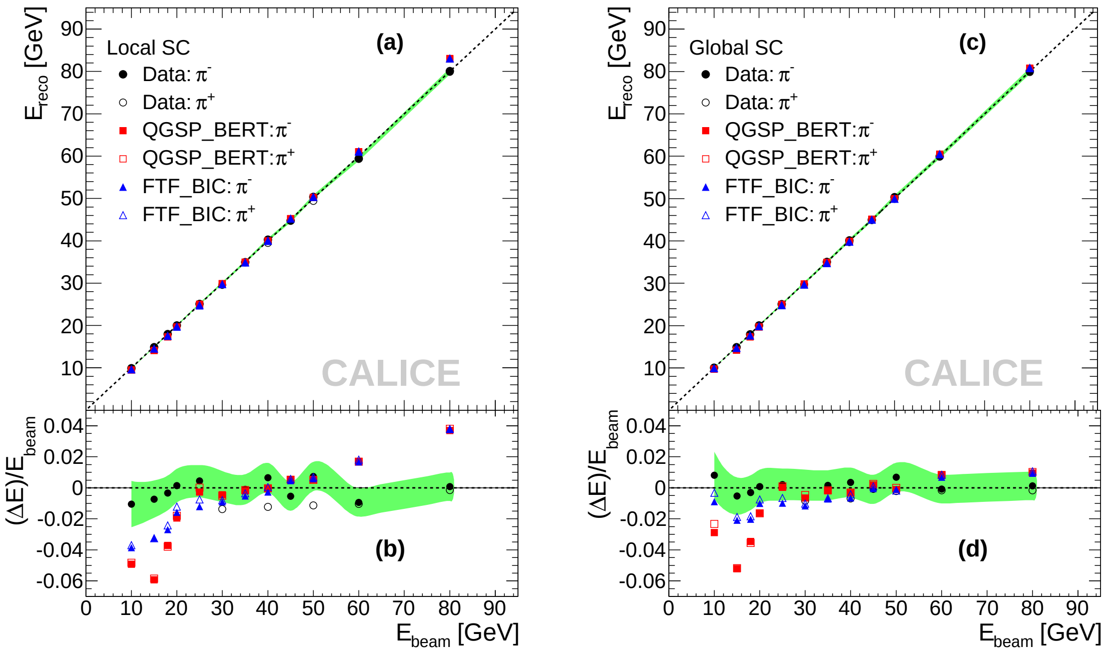

Figure 11. Detector response to pions with software compensation comparing data and simulations. For both data and simulations compensation parameters derived from data are used. (a) Response with local software compensation and (b) corresponding relative residuals to beam energy. (c) Response with global software compensation and (d) corresponding relative residuals to beam energy.

tion of software compensation results in an improved response linearity and in a better agreement between data and simulations for both physics lists considered. At higher energy, a significant overestimation of the reconstructed energy by simulations is seen with local software compensation, while the global software compensation technique successfully corrects the non-linearity of the simulations in that energy regime. This difference in behavior is partially due to uncertainties in the treatment of saturation effects in simulations, and potentially also receives contribution from imperfect descriptions of the shower structure by the shower models themselves. In the simulations, the number of cells with very high energy content is overestimated and exhibits a longer tail than in data. This affects the correction factor of the global software compensation by construction, resulting in a on average lower shower weight for simulations compared to data at the same energy, bringing data and simulations into better agreement. The local software compensation technique applies constant weights for very high-energy hits, as can be seen in Figure 5. It is thus less sensitive to these differences between data and simulations and preserves the discrepancy in visible energy for high beam energies.

Figure 12 shows the energy resolution for simulations compared to that for data for both software compensation techniques. The local software compensation largely preserves the differences between data and simulations for the physics list QGSP_BERT, but results in a better agreement of FTF_BIC with data, in agreement with the behavior observed for the reconstructed energy. The global software compensation brings the overall trend of the resolution with energy for data and

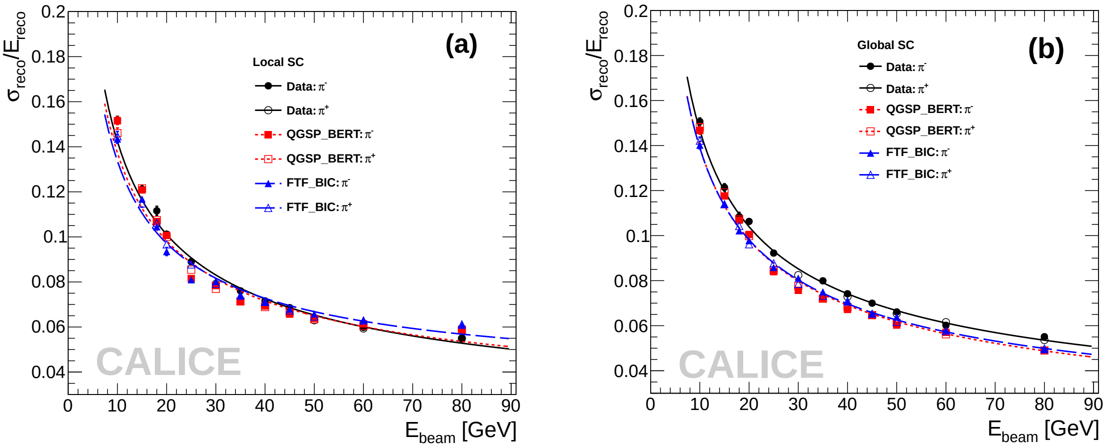

Figure 12. Relative energy resolution for pions with local (a) and global (b) software compensation comparing data and simulations. For both data and simulations compensation parameters derived from data are used. The curves show fits using Equation 2.2. The fit results for the local software compensation are $(44.3 \pm 0.3)\%$, $(42.3 \pm 0.2)\%$ and $(40.4 \pm 0.3)\%$ for the stochastic term, with constant terms of $(1.8 \pm 0.2)\%$, $(2.5 \pm 0.1)\%$ and $(3.4 \pm 0.1)\%$ for data, QGSP_BERT and FTF_BIC, respectively. For the global software compensation, the results are $(45.8 \pm 0.3)\%$, $(43.6 \pm 0.2)\%$ and $(43.4 \pm 0.3)\%$ for the stochastic term, with constant terms of $(1.6 \pm 0.2)\%$, $(0.0 \pm 0.2)\%$ and $(1.1 \pm 0.2)\%$ for data, QGSP_BERT and FTF_BIC, respectively.

simulations into good agreement, with better resolution seen for simulations with both physics lists than for data.

The relative improvement in resolution compared to the uncorrected energy resolution is shown in Figure 13 for data and simulations. For the local software compensation, the improvement with respect to energy observed in data is well reproduced by the QGSP_BERT physics list. For FTF_BIC, a considerably bigger improvement is seen for the simulations at high energy than is seen in data. This higher improvement at high energies results in the better agreement of the energy resolution in data and in simulations discussed above. For the global compensation approach, the behaviour up to 30 GeV is well modelled, while an up to 20% higher improvement, compared to that for data, is seen in simulations at the highest energies considered. The reason for this different behavior of local and global software compensation is the same which also leads to the different high-energy behavior of the reconstructed energy discussed above, namely a difference in the distribution of very high-energy hits. This results in a difference in potential resolution improvements for data and simulations depending on the sensitivity of the chosen technique to this type of calorimeter hits.

5. Conclusion

The hadronic energy resolution of the CALICE analogue hadron calorimeter is studied using test beam data collected in 2007 at the CERN SPS. The calorimeter, with an instrumented volume of approximately 1 m^3 and a depth of 5.3 λ_I, is highly segmented in both longitudinal and lateral

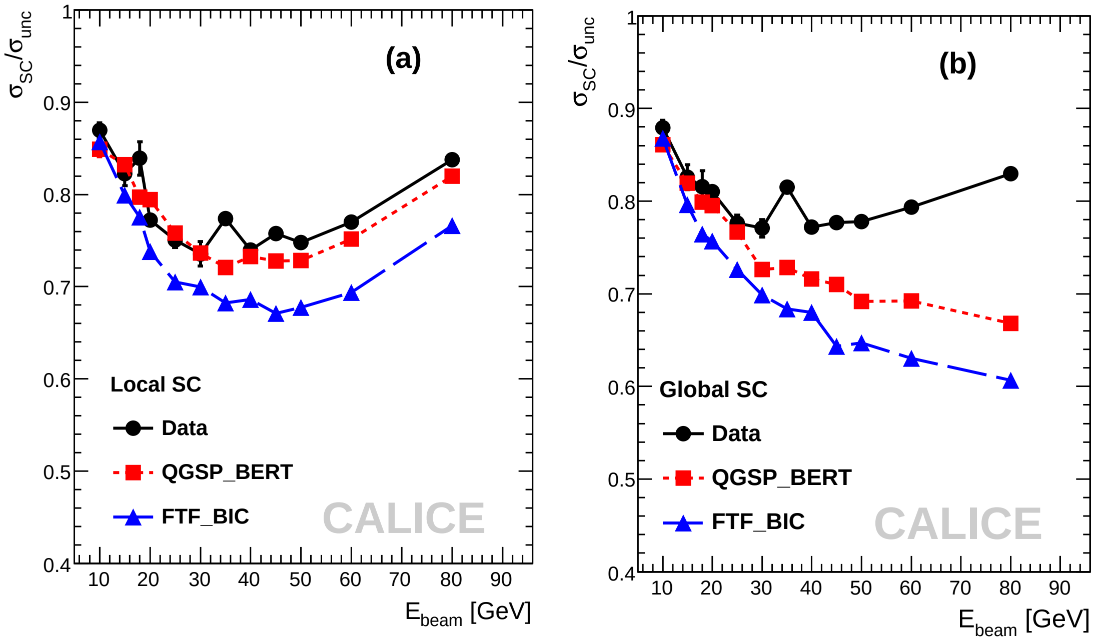

Figure 13. Energy dependence of the relative improvement of the resolution for data and simulations using the physics lists QGSP_BERT and FTF_BIC, (a) with local software compensation and (b) with global software compensation. Where available, results for π^- and π^+ are averaged for clarity.

direction, with a total of 7608 electronic channels. The intrinsic energy resolution of the CALICE AHCAL for hadrons is measured to be $58\%/\sqrt{E/\mathrm{GeV}}$, with a constant term of 1.6%.

The unprecedented granularity of the CALICE AHCAL provides excellent possibilities for the application of software compensation algorithms to improve the energy resolution of the calorimeter based on event-by-event information on the energy density structure of the showers. Two techniques have been presented here, together with results on test beam and on simulated data samples. The local software compensation technique uses local energy density information for a cell-by-cell re-weighting of energy deposits, while the global software compensation technique uses the distribution of cell energies to derive one overall weighting factor for each shower. Both techniques show similar performance, with a relative improvement of the energy resolution ranging from 12% to 25% over the studied energy range from 10 GeV to 80 GeV, resulting in a reduction of the stochastic term to $45\%/\sqrt{E/\mathrm{GeV}}$. In GEANT4 simulations with the QGSP_BERT and the FTF_BIC physics lists, the detector response is considerably more non-linear than in data. The physics list QGSP_BERT provides a satisfactory description of the energy resolution. The application of software compensation using parameters determined from data brings the resolution into better agreement with data. Here, the improvement of the energy resolution using the local software compensation technique observed for the QGSP_BERT physics lists is comparable to that observed for data, while larger differences are observed for FTF_BIC and for the global software compensation technique.

Neither of the described techniques requires an a priori knowledge of the particle energy.

The energy dependent compensation factors are selected based on the uncorrected reconstructed energy. Although this energy dependence places some restrictions on the implementation of both techniques in a collider environment with a high particle density in hadronic jets, their application in the context of particle flow algorithms should be possible based on identified calorimeter clusters.

Acknowledgments

References

[1] J. Brau, (Ed.) *et al.* [ILC Collaboration], *ILC Reference Design Report: ILC Global Design Effort and World Wide Study*, arXiv:0712.1950 [physics.acc-ph].

[2] R. W. Assmann *et al.*, *A 3-TeV e^+e^- linear collider based on CLIC technology*, CERN-2000-008.

[3] J. -C. Brient and H. Videau, *The calorimetry at the future e^+e^- linear collider*. eConf C **010630** (2001) E3047 [hep-ex/0202004].

[4] V. L. Morgunov, *Calorimetry design with energy-flow concept (imaging detector for high-energy physics*, Proc. of Calorimetry in Particle Physics (CALOR 2002), pp. 70-84, Pasadena, California, 25th-29th Mar. 2002.

[5] M. A. Thomson, *Particle Flow Calorimetry and the PandoraPFA Algorithm*, Nucl. Instrum. Meth. **A 611** (2009) 25.

[6] C. Adloff, *et al.* [CALICE Collaboration], *Study of the interactions of pions in the CALICE silicon-tungsten calorimeter prototype*, JINST **5** (2010) P05007.

[7] C. Adloff, *et al.* [CALICE Collaboration], *Tests of a particle flow algorithm with CALICE test beam data*, JINST **6**, (2011) P07005.

[8] C. Adloff *et al.* [CALICE Collaboration], *Construction and Commissioning of the CALICE Analog Hadron Calorimeter Prototype*, JINST **5** (2010) P05004.

[9] J. Repond *et al.* [CALICE Collaboration], *Design and Electronics Commissioning of the Physics Prototype of a Si-W Electromagnetic Calorimeter for the International Linear Collider*, JINST **3** (2008) P08001.

[10] C. Adloff *et al.* [CALICE Collaboration], *Construction and performance of a silicon photomultiplier/extruded scintillator tail-catcher and muon-tracker*, JINST **7** (2012) P04015.

[11] C. Adloff *et al.* [CALICE Collaboration], *Response of the CALICE Si-W electromagnetic calorimeter physics prototype to electrons*, Nucl. Instrum. Meth. **A 608** (2009) 372.

[12] C. Adloff *et al.* [CALICE Collaboration], *Electromagnetic response of a highly granular hadronic calorimeter*, JINST **6** (2011) P04003.

[13] C. W. Fabjan *et al.*, *Iron Liquid - Argon and Uranium Liquid - Argon Calorimeters for Hadron Energy Measurement*, Nucl. Instrum. Meth. **141** (1977) 61.

[14] T. A. Gabriel *et al.*, *Energy dependence of hadronic activity*, Nucl. Instrum. Meth. A **338** (1994) 336.

[15] M. Derrick *et al.*, *Design and construction of the ZEUS barrel calorimeter*, Nucl. Instrum. Meth. **A 309** (1991) 77.

[16] A. Andresen *et al.*, *Construction and beam test of the ZEUS forward and rear calorimeter*, Nucl. Instrum. Meth. **A 309** (1991) 101.

[17] G. d'Agostini *et al.*, *Experimental Study Of Uranium Plastic Scintillator Calorimeters*, Nucl. Instrum. Meth. **A 274** (1989) 134.

[18] H. Abramowicz *et al.*, *The Response And Resolution Of An Iron Scintillator Calorimeter For Hadronic And Electromagnetic Showers Between 10 GeV And 140 GeV*, Nucl. Instrum. Meth. **180** (1981) 429.

[19] B. Andrieu *et al.*, *Results from pion calibration runs for the H1 liquid argon calorimeter and comparisons with simulations*, Nucl. Instrum. Meth. **A 336** (1993) 499.

[20] C. Cojocaru *et al.*, *Hadronic calibration of the ATLAS liquid argon end-cap calorimeter in the pseudorapidity region 1.6* $< |\eta| <$ *1.8 in beam tests*, Nucl. Instrum. Meth. **A 531** (2004) 481.

[21] S. Agostinelli *et al.* [GEANT4 Collaboration], GEANT4*: A Simulation toolkit*, Nucl. Instrum. Meth. **A 506** (2003) 250.

[22] A. Ribon *et al.*, *Status of* GEANT4 *hadronic physics for the simulation of LHC experiments at the start of LHC physics program*, CERN-LCGAPP-2010-002 (2010).